

# Dynamics of subduction initiation at preexisting fault zones

John Toth<sup>1</sup> and Michael Gurnis

Seismological Laboratory, California Institute of Technology, Pasadena

**Abstract.** We show that a new subduction zone can initiate at a preexisting dipping fault zone with reasonable plate forces, consistent with what is observed in the western Pacific. The dynamics of subduction initiation within a viscoelastic medium has been systematically explored with the finite element method. We investigate the compression of oceanic lithosphere with both force and velocity boundary conditions and track the thermal structure in which heat is transported by both advection and diffusion. The viscosity of the medium is non-Newtonian and temperature-dependent. We also examine the influence of a perfectly plastic yield stress. A new method to model the preexisting weak zone as a graded fault with remeshing is introduced. The first 400 km of plate convergence is examined during which time there are profound changes in plate boundary dynamics. Initially, topography across the plate boundary is characterized by over 1000 m of uplift close to the trench. Subsequently, a bathymetric depression develops on the overriding plate with an initial subsidence rate of 125 m/Myr for a slab subducting at 2 cm/yr. Tectonic subsidence of the overriding plate is primarily dependent upon the depth of slab penetration. For a plate force of  $4 \times 10^{12}$  N/m, subduction initiates even with a fault shear stress of 3 MPa, the resistance most consistent with seismological observations. However, subduction will not initiate when this fault shear stress is  $>5$  MPa. Our results are consistent with plate reconstructions, which predict the initiation of subduction across preexisting weak zones within oceanic basins.

## 1. Introduction

Subduction initiation, although only a transient phenomenon, is a vital phase of the plate tectonic cycle. Long-lived and well-developed subduction zones disappear as the Cenozoic demise of subduction off California shows, and consequently new subduction zones must form. Many theoretical studies, most recently *Mueller and Phillips* [1991], have concluded that subduction initiation is extraordinarily difficult despite the fact that it must occur regularly during the normal evolution of plate tectonics. The earliest phases of convergence and subduction must be associated with large changes in the force balance of subducting and overriding plates, particularly the slab pull force, which should rapidly increase as the slab descends into the mantle. Unfortunately, since active plate margins are often consumed by the normal plate tectonic cycle, there is only limited observational evidence of this process. Although several studies have examined the initiation of subduction [*McKenzie*, 1977; *Karig*, 1982; *Casey and Dewey*, 1984; *Cloetingh et al.*, 1989; *Mueller and Phillips*, 1991; *Stern and Bloomer*, 1992; *Kemp and Stevenson*, 1996], the dynamics of this process remain poorly understood. If the process must occur regularly and continuously, then something must be wrong with previous models to arrive at the conclusion that subduction cannot initiate with known forces.

In order to shed greater light on this problem and to overcome substantial limitations in past theoretical

approaches, we have developed a realistic numerical model to investigate the dynamics of subduction initiation. By comparing our model results with the early geology and tectonic history of convergent plate boundaries we aim to develop a greater understanding of subduction initiation. We are particularly interested in the response of the overriding plate to the initiation of subduction and how this response varies both spatially and temporally as a new subducting slab develops. We consider the history of a plate boundary for the first 400 km of relative plate convergence, by which time the slab is well developed, but before the slab crosses the 410 km phase change. The model can be constrained by topography and tectonics of the overriding plate, Benioff zone geometry, earthquake focal mechanisms, plate velocities, and trench topography. Where subduction has initiated close to a continental margin, as in the Cenozoic subduction beneath the North Island of New Zealand, a geological record may be left, which preserves the history of initiation [*Kamp*, 1984; *Stern and Holt*, 1994]. In this case, sedimentary basin stratigraphy and subsidence rates offer a time-dependent record which better constrains initiation dynamics compared to present-day observations, which provide only a "snapshot" of the process.

From Mesozoic and Cenozoic plate reconstructions of the western Pacific it is clear that changes in relative plate motion across preexisting transform faults and fracture zones can lead to the formation of new convergent plate boundaries [*Uyeda and Ben-Avraham*, 1972]. *Hilde et al.* [1977] suggested that the Philippine, Bonin-Mariana, and Tonga trench-arc systems initiated along three major N-S transform faults at  $\sim 45$  Ma, leading to entrapment of oceanic crust within the West Philippine Sea basin and also possibly within the South Fiji basin. At  $\sim 65$  Ma the Aleutian trench may have initiated along an E-W fracture zone, entrapping the Bering Sea basin [*Hilde et al.*, 1977; *Scholl et al.*, 1975], where magnetic lineations are perpendicular to the strike of the Aleutian trench [*Copper et al.*, 1976]. *Stern and Bloomer* [1992],

<sup>1</sup>Now at Shell International Exploration and Production, Rijswijk, Netherland.

Copyright 1998 by the American Geophysical Union.

Paper number 98JB01076.  
0148-0227/98/98JB-01076\$09.00

proposed that both the Eocene Bonin-Mariana and the Jurassic California arcs may have formed in a similar way; subduction is initiated along a transform plate boundary separating lithosphere of contrasting age.

The East Caroline plate in the western Pacific, north of New Guinea, may be a site of present day subduction initiation. The boundary between the eastern Caroline plate and the Pacific plate shows convergence, which varies in style and magnitude along strike [Hegarty *et al.*, 1982]. At the southern end of the plate boundary the Caroline plate is underthrusting the Pacific at the Mussau trench, whereas in the north the Caroline plate is overriding the Pacific plate. Hegarty *et al.* [1982] estimate a maximum of 11 km of shortening at 1.6 cm/yr, initiating ~700,000 years ago. They suggest that convergence began along a zone of weakness delineated by a preexisting fracture zone within the Caroline plate. Bathymetric profiles show a 7000 m deep trench axis flanked by a 2000 m deep ridge ~35 km to the east [Hegarty *et al.*, 1982]. Another example of an incipient subduction zone along a transform plate boundary is the Puysegur ridge and trench at the northern end of the Macquarie ridge complex [Collot *et al.*, 1995]. Oblique convergence occurs along the Puysegur ridge where subduction is propagating southwards along the strike slip boundary. Earthquake focal mechanisms show a trench-parallel sub-vertical strike-slip fault beneath the ridge axial valley, and a southeastward, shallow dipping oblique thrust [Collot *et al.*, 1995]. The development of the subduction zone was facilitated by the development of reverse faults, which accommodate the normal convergence [Collot *et al.*, 1995].

Casey and Dewey [1984], in an examination of subduction initiation and ophiolitic geology, proposed that the evolution of transform plate boundaries into trenches explains many of the features of obducted ophiolites. Orogenic activity at continental margins is often initiated by overthrusting and obduction toward the previously stable margin. This indicates that subduction polarity was away from the continental margin, and that the trench nucleation was intra-oceanic. Therefore Casey and Dewey [1984] propose that upon changes in poles of relative plate motion, subduction zones have a strong tendency to initiate within ocean basins by the conversion of preexisting plate boundaries to subduction zones. It is the dynamics of this process that we study here.

In an influential paper, McKenzie [1977] estimated the minimum force required for a finite instability of the oceanic lithosphere to grow and for subduction to initiate. In this simple model ridge push and slab pull are resisted by friction on the fault and resistance to plate bending. If the shear stress across the fault is 10 MPa, McKenzie [1977] found that subduction would be initiated with a force of at least  $6.4 \times 10^{12}$  N/m. After the slab reached a depth of 130 km subduction would be self sustaining. McKenzie [1977] estimated ridge push to be  $4 \times 10^{12}$  N/m and concluded that subduction would be difficult, but not impossible, to start. McKenzie [1977] argued that this difficulty to initiate subduction is not inconsistent with plate tectonics, since plates themselves are large (have a large-aspect ratio) and trenches are relatively rare. More recently, Mueller and Phillips, [1991] have carried out a more systematic, but similar, analysis to McKenzie [1977] but concluded that subduction would be almost impossible to initiate. In most cases studied, the force necessary to overcome the strength of the lithosphere would be nearly 1 order of magnitude larger than known ridge push. McKenzie [1977] assumed that the stress on preexisting faults would be less than ~10 MPa, while Mueller and Phillips, [1991] directly applied experimental rock mechanics results and assumed that preexisting faults nearly follow Byerlee's law and have shear stresses substantially >100 MPa.

However, we will show here that the recorded conversion of preexisting transform boundaries to subduction zones, as observed in the geological record within the western Pacific, indicates that frictional resistance along these boundaries does not preclude trench initiation, and the frictional resistance along the fault must be <10 MPa. In the model presented here the resistance to subduction comes from elastic resistance to deflection of both the subducting and overriding plates, from viscous resistance to the slab penetrating the mantle, from plate drag as the subducting lithosphere moves over the asthenosphere, and from frictional stresses on a dipping fault. Moreover, by simultaneously solving for transport of heat, we are able to study the limiting influence of diffusion on the growth of slab buoyancy, which is particularly important for slowly nucleating margins. We estimate the forces necessary to initiate subduction.

## 2. The Model

For a well-developed converging margin, sophisticated numerical models have been used to reconcile subduction dynamics with the tectonics of the overriding plate [e.g., Bott *et al.*, 1989; Wdowinski and O'Connell, 1991; Gurnis, 1992; Wdowinski and Bock, 1994; Zhong and Gurnis, 1994]. However, the early history of subduction and tectonics has been largely neglected for newly nucleating subduction zones. We have developed a two-dimensional thermal advection-diffusion model with a viscoelastic rheology and have investigated this early history. The finite element method with the displacement approach [Zienkiewicz, 1977] is used with linear triangular elements. The solution is formulated in terms of the conservation of work, equating the external work done by nodal forces with internal work done by the element stresses. The model has been designed specifically to investigate subduction initiation. The time scale of the problem, ~ 0 - 20 Myr, and its transient nature indicate that both elastic and viscous strains will be significant and that the appropriate constitutive equation is for Maxwell viscoelasticity. Stress is propagated elastically and produces flow by viscous power law creep. The general solution is one for linear elasticity with infinitesimal strain. However, this has been modified to accommodate viscous creep and large displacements with the inclusion of initial strain and initial stress vectors and using an iterative incremental approach [Zienkiewicz, 1977; Wallace and Melosh, 1994]. At the end of each time increment, the nodal positions are updated by the nodal displacements, and a new stiffness matrix is constructed. The stress tensor at the end of the previous time step is then incorporated as an initial stress term,  $\sigma_0$ , for the next time step [Wallace and Melosh, 1994]. The deviatoric stress tensor is used to calculate the viscous strain for the next time step, which is incorporated as an initial strain term,  $\epsilon_0$ , [Zienkiewicz, 1977]. For each time step, the relation between stress and strain is

$$\sigma = D(\epsilon - \epsilon_0) + \sigma_0 \quad (1)$$

where  $D$  is the constitutive elasticity matrix for plane strain as follows:

$$\begin{bmatrix} \sigma_{xx} \\ \sigma_{yy} \\ \sigma_{xy} \end{bmatrix} = \frac{E(1-\nu)}{(1+\nu)(1-2\nu)} \begin{bmatrix} 1 & \frac{\nu}{(1-\nu)} & 0 \\ \frac{\nu}{(1-\nu)} & 1 & 0 \\ 0 & 0 & \frac{(1-2\nu)}{2(1-\nu)} \end{bmatrix} \begin{bmatrix} \epsilon_{xx} \\ \epsilon_{yy} \\ \gamma_{xy} \end{bmatrix} \quad (2)$$

where  $\nu$  is Poisson's ratio,  $E$  is Young's modulus,  $\epsilon$  is the strain, and  $\gamma_{xy} = 2\epsilon_{xy}$ . The elastic stress is then used to determine the viscous strain for the proceeding time step. The constitutive equation we have used for the viscous strain,  $\epsilon_v$ , is

$$\begin{bmatrix} \epsilon_{xx} \\ \epsilon_{yy} \\ \gamma_{xy} \end{bmatrix} = \Delta t \frac{A\sigma_E^{(n-1)}}{4\eta_T} \begin{bmatrix} 1 & -1 & 0 \\ -1 & 1 & 0 \\ 0 & 0 & 4 \end{bmatrix} \begin{bmatrix} \sigma_{xx} \\ \sigma_{yy} \\ \sigma_{xy} \end{bmatrix} \quad (3)$$

where  $n=3$ ,  $\Delta t$  is the time step,  $\eta_T$  is the temperature-dependent viscosity,  $\sigma_E$  is the second-order invariant of the deviatoric stress [Melosh and Raefsky, 1980; Ranalli, 1995] and the preexponent  $A = 10^{-13}/\text{Pa}^2$ . The viscous strain for each time step must be less than the elastic strain and, for the low effective viscosity within the upper mantle of our model, this limits  $\Delta t$  to  $\sim 50$  years. The temperature dependent viscosity (Figure 1) is given by

$$\eta_T = \eta_m \exp\left[\frac{Q}{R}\left(\frac{1}{T} - \frac{1}{T_m}\right)\right] \quad (4)$$

where  $Q$  is the activation energy,  $R$  is the gas constant, and  $\eta_m$  and  $T_m$  are the viscosity and temperature of the half-space below the lithosphere, respectively [Courtney and Beaumont, 1983]. Courtney and Beaumont [1983] showed that this simple thermal parameterization could reconcile estimates of effective elastic thickness from both thermal models and thin elastic plate models. They found that the effective elastic thickness derived from viscoelastic models with  $Q = 170$  kJ/mol matched observations of the flexure of oceanic lithosphere with thermal ages ranging from 0 to 200 Ma [Watts et al., 1980]. If the activation energy was larger than this, 350 kJ/mol is usually used to model the creep of the upper mantle, then the effective elastic thickness of the oceanic lithosphere would be much too high and inconsistent with observations. The initial temperature field is determined from the cooling of a semi-infinite half-space [Turcotte and

Schubert, 1982]. The thermal advection and diffusion is solved using the finite difference method. We used the central difference approximation, with upwind differencing on the advective term to remove oscillations associated with rapid changes in downstream boundary conditions [e.g., Brooks, 1981].

Plasticity has been incorporated into the model via the initial stress tensor,  $\sigma_0$ . If the maximum shear stress exceeds a specified plastic yield stress,  $\tau_{\text{yield}}$ , then the principal stresses are reduced, keeping the pressure constant, to bring the shear stress back within the failure envelope. Upon removal of the load, only the elastic strain is recovered.

The left, right, and bottom boundaries of the model are free slip (Figure 1). The top boundary is a free surface with vertical isostatic restoring forces [Wallace and Melosh, 1994], and any topography is water filled. In order to understand subduction initiation it is important to examine the processes in the context of a large scale geodynamic setting. The model extends to 1000 km depth, deep enough to include a change in viscosity at the 670 km transition, and has a width of 4000 km (Figure 1). Below 670 km the viscous constitutive equation is linear with  $\eta = 5 \times 10^{21}$  Pa s, a value consistent with postglacial rebound and studies of the geoid [Forte and Mitrovica, 1996].

Within the center of the box, a preexisting fault cutting the lithosphere is included as a discontinuity (Figure 1). The fault is modeled as a discrete boundary, which is defined by a shear stiffness and a normal stiffness (modified from Goodman et al., [1968]). The stiffness is simply the ratio between nodal force and nodal displacement. The normal stiffness is set high enough ( $10^{13}$  N/m) so that there is zero displacement normal to the fault ( $U = 0$ , Figure 2a). The shear stiffness is effectively the amount of shear coupling between the opposing fault surfaces and controls the shear stress on the fault plane. In an initial set of models, we define the fault to be completely uncoupled within the lithosphere, where the shear stiffness on the fault plane is zero. The shear stiffness increases as  $\tanh(z)$  until the fault becomes fully locked at depth (Figure 2b). In this way we avoid having an abrupt fault tip within the upper mantle; the relative displacement across the fault gradually decreases to zero with depth as the shear

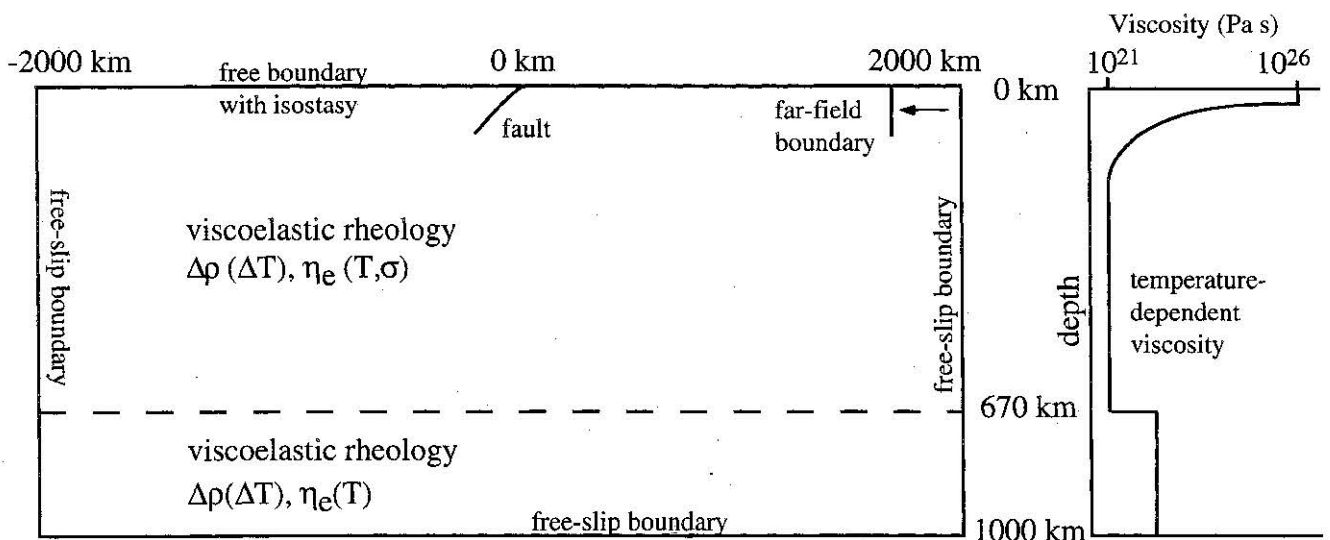


**Figure 1.** Schematic representation of the model. Left, right, and bottom boundaries are free slip. Top boundary is free surface with isostatic restoring forces. The rheology is viscoelastic. The constitutive equation for viscous creep is nonlinear above 670 km depth,  $n = 3$ . Below 670 km the constitutive equation is linear. Viscosity is temperature dependent with a maximum cutoff effective viscosity of  $10^{26}$  Pa s.

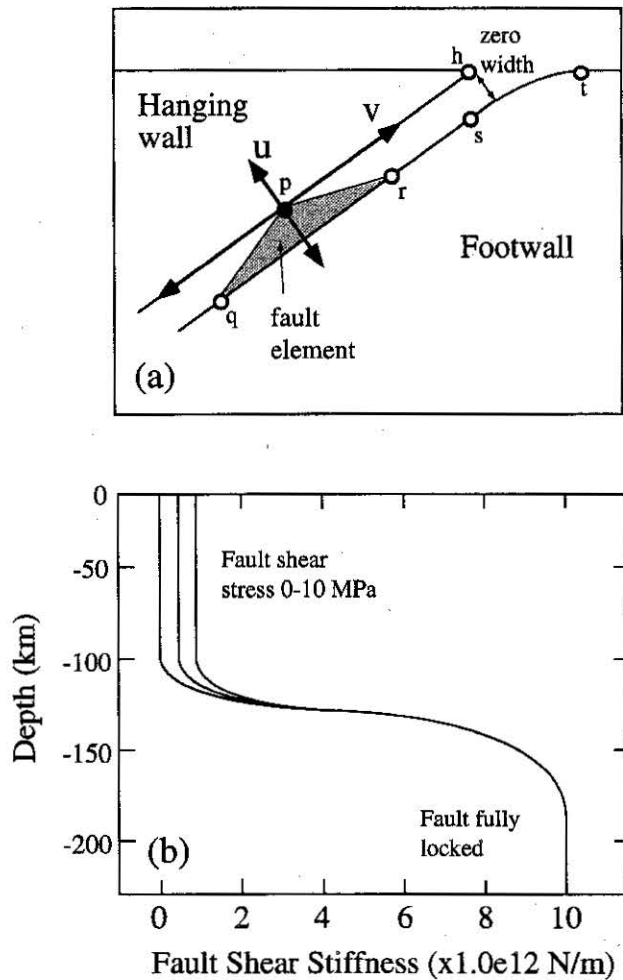


**Figure 2.** The mechanics of the fault construction. (a) The fault stiffness relates nodal forces to nodal displacements. The normal stiffness is set high enough so that  $U = 0$ . The shear stiffness is effectively the amount of shear coupling across the fault and controls the displacement parallel to the fault plane,  $V$ . (b) The shear stiffness is zero, or low, within the lithosphere and increases with depth until the fault becomes fully locked. The relative displacement across the fault is thereby gradually reduced to zero with depth.

stiffness on the fault increases. The discontinuous brittle deformation is gradually replaced by continuous viscoelastic strain. The inclusion of the fault in this manner is a critical component of the model. In a single model it allows us to integrate the elastic/brittle nature of lithosphere deformation with the more viscous mantle deformation. The formulation of the fault in this manner allows us to avoid the problem, observed in some previous Lagrangian models [e.g., *Melosh and Williams, 1989*], of voids opening at the fault tip after large displacements. As the displacement across the fault increases, the fault elements become distorted. In Figure 2a the fault element has nodes  $p$ ,  $q$ , and  $r$ . When node  $p$  passes node  $r$ , the fault element is flipped and node  $p$  is reconnected to nodes  $r$  and  $s$  and subsequently to nodes  $s$  and  $t$ . In this way the hanging wall and footwall remain in contact for large displacements. Moreover, the node  $h$ , defining the fault tip on the hanging wall, is always in contact with the surface of the lower footwall.

When we refer to "fault coupling," it is important to distinguish between long-term and short-term deformation. Long-term deformation is on a time-scale greater than the characteristic recurrence interval for fault movements on major faults [*Walcott, 1984*]. *Walcott* [1984] estimated a

recurrence time of 1000 years for major fault movements within New Zealand and proposed that long-term deformation be defined as  $>10,000$  years, over which time there will be many fault ruptures. For the models presented here, with a timescale much  $>1000$  years and low rates of convergence, it may be considered that the subduction fault is effectively unlocked. We initially investigate models with zero shear stress on the subduction fault and then examine the influence of increasing the amount of shear stress.

We use a Lagrangian formulation. When the finite element mesh becomes too distorted, we regrid the mesh around the fault plane and the top surface of the model and linearly interpolate the stress onto the new grid. The interpolation is aided by the fact that our material parameters are temperature-dependent. Viscosity and density change gradually, reflecting the diffuse temperature field. Moreover, there are no material boundaries within the model so that interpolation offers no major problems. We have systematically explored the accuracy and resolution of our models. The code has been extensively benchmarked against analytic solutions and with solutions from the finite element code Tecton [*Melosh and Raefsky, 1980*] in the limit of large displacements and long integrations of time. We demonstrate the convergence and stability of our code in section 3.1.

It is envisaged that subduction is initiated across preexisting weak zones due to changes in plate kinematics. This may occur following changes in the nature of specific plate boundaries; for example, subduction may terminate because of collision of a continent with a trench or slab pull may be reduced because of subduction of a spreading ridge. The resultant far field force acting on a plate is incorporated into the model by specifying a far field plate boundary (Figure 1), on which we prescribe either a constant velocity or a constant force. The boundary is a vertical plane through the lithosphere, with a depth of 90 km, which initially lies 1750 km from the trench. After 400 km of plate convergence the boundary has moved horizontally to a position 1350 km from the trench. Between the far field boundary and the right wall of the model lies a weak zone which has the same viscosity as the upper mantle. As the far field boundary moves toward the trench, a cavity flow develops, and material from the mantle flows back into the weak zone. Consequently, our Lagrangian model has many similarities to mantle convection models in which a purely viscous rheology is solved with an Eulerian method [e.g., *Gurnis and Hager, 1988*]. Initially, the only driving force is from the far field boundary condition; however, as the slab develops, the dynamics of the model will shift from predominantly ridge push to predominantly slab pull.

### 3. Results

Our aim is to understand the changing dynamic interaction between the subducting and overriding plates during subduction initiation and the corresponding evolution of topography and tectonic stress across the plate boundary. We investigate the influence of plate convergence velocity, plate driving force, plate age, mantle viscosity, fault geometry, plastic failure within the upper lithosphere, and fault shear stress. We compare constant velocity boundary condition models with constant force boundary condition models and determine the minimum force required to initiate subduction for models with different shear stresses on the fault.

#### 3.1. Reference Model

We first present model A, which incorporates a realistic set of thermorheological parameters (Table 1). A constant far field plate convergence velocity of 2 cm/yr is imposed, the thermal age of the lithosphere is 80 Ma, and the shear stress

**Table 1.** Thermo-Rheological Parameters for Model A

Parameter	Value
Thermal age of lithosphere	80 Myr
Maximum effective viscosity	$1 \times 10^{26}$ Pa s
Minimum effective viscosity	$6 \times 10^{20}$ Pa s
Effective viscosity below 670m	$5 \times 10^{21}$ Pa s
Activation energy	170 kJ mol <sup>-1</sup>
Coefficient of thermal expansion	$3.28 \times 10^{-5}$ K <sup>-1</sup>
Thermal diffusivity	$1.0 \times 10^{-6}$ m <sup>2</sup> s <sup>-1</sup>
Young's modulus	$1.6 \times 10^{11}$ Pa
Poisson's ratio	0.3
Shear stress on lithosphere fault	zero
Plate convergence velocity	2 cm yr <sup>-1</sup>

across the lithospheric fault is zero. The model is integrated forward for 20 Myr, by which time there has been 400 km of plate convergence (Figure 3). After 20 Myr, the 1200°C isotherm, defining the base of the lithosphere, has been deflected into the mantle to a depth of nearly 350 km (Figure 3b). The velocities are constant within the slab at 2 cm/yr, while the velocity vectors within the overriding plate nearly vanish. Above 100 km depth there is no shear coupling between the slab and the overriding plate; the fault is completely unlocked. Below 100 km the coupling gradually increases, producing flow within the asthenosphere and a clockwise rotation at the slab tip. After 5 Myr, and 100 km of convergence, the horizontal deviatoric compressional stress within the plate interior, 800 km from the trench, is ~85 MPa (Figure 4a). Close to the trench, the horizontal deviatoric stresses within the upper lithosphere of the subducting plate are strongly extensional, reaching values of ~130 MPa. However, at a depth of 30 km the horizontal stresses become compressional, as would be expected from the bending of an elastic plate of ~50 km (Figure 4a). After 20 Myr, and 400 km of convergence, the horizontal deviatoric stresses within the subducting plate, away from the trench, become entirely extensional (Figure 4b). Although the far field boundary is still converging toward the trench at 2 cm/yr, the constant velocity boundary now acts to hinder subduction. Close to the trench, horizontal compression is seen at a depth of 50 km, the slab pull force has increased the depth of the neutral surface which separates extensional bending stresses in the upper part of the elastic plate from compressional bending stresses in the lower part of the elastic plate. Within the overriding plate, above the lithosphere fault, the horizontal deviatoric stresses are compressional, with a maximum deviatoric stress of ~85 MPa, 250 km from the trench (Figure 4b). At ~400 km from the trench, close to the slab tip, the horizontal stress within the overriding plate becomes extensional. Within the slab, at ~75 km depth, it can be seen that the stress has changed from down dip compression at 5 Myr to down dip extension at 20 Myr.

An examination of time evolution of this standard case shows that on the overriding plate, close to the trench, there is over 1000 m of initial uplift (Figure 5a). This is due to the thrusting of the hanging wall over the footwall. Subsequently, as the slab develops, the trench bathymetry increases from nearly 4000 m at 5 Myr to nearly 6000 m at 20 Myr. During the same time interval a depression has developed in the overriding plate which broadens and deepens with time and reaches a maximum bathymetry of nearly 4000 m after 20 Myr (Figure 5a). Subsidence plots for the

overriding plate show that uplift, 50 km from the trench, reaches a maximum of 1250 m after ~7.5 Myr of convergence (Figure 5b). The average subsidence rate 250 km from the trench is 190 m/Myr.

In order to test the sensitivity of the model to changes in grid resolution, we produced a test model which was identical to model A, but in which the number of finite elements was doubled from 4600 to 9200. The high resolution test model was integrated for 20 Myr, by which time there had been 400 km of plate convergence. The resulting topography (Figure 5c) and fault geometry (Figure 5d) are essentially identical to model A. The high resolution model produced a sharper topographic profile very close to the trench but it was found that model A is well resolved. This test also indicates that the regridding and interpolation routine is not influenced by a further increase in grid resolution. In all subsequent cases we will use a mesh with 4600 elements.

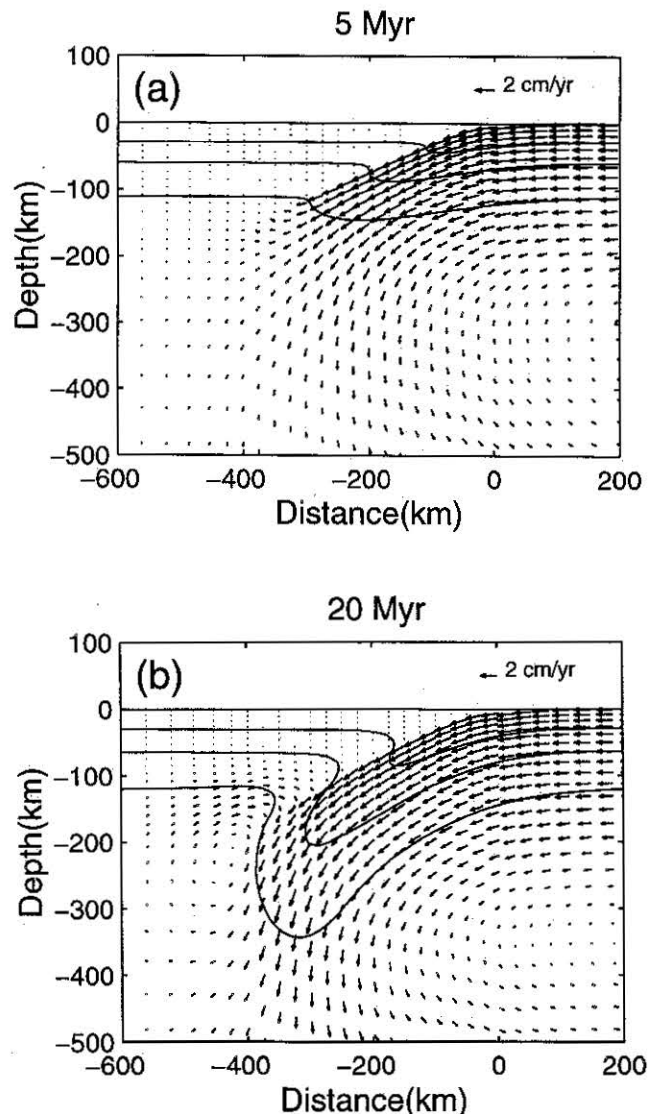


**Figure 3.** Temperature contours (isotherms at 400°C intervals) and velocity vectors for Model A, for a small region near the nucleating slab; the entire domain is 4000 km x 1000 km. (a) After 5 Myr and (b) after 20 Myr of plate convergence at a rate of 2 cm/yr. Within the overriding plate the velocities are almost zero. Clockwise circulation can be seen within the asthenosphere wedge, close to the slab tip.

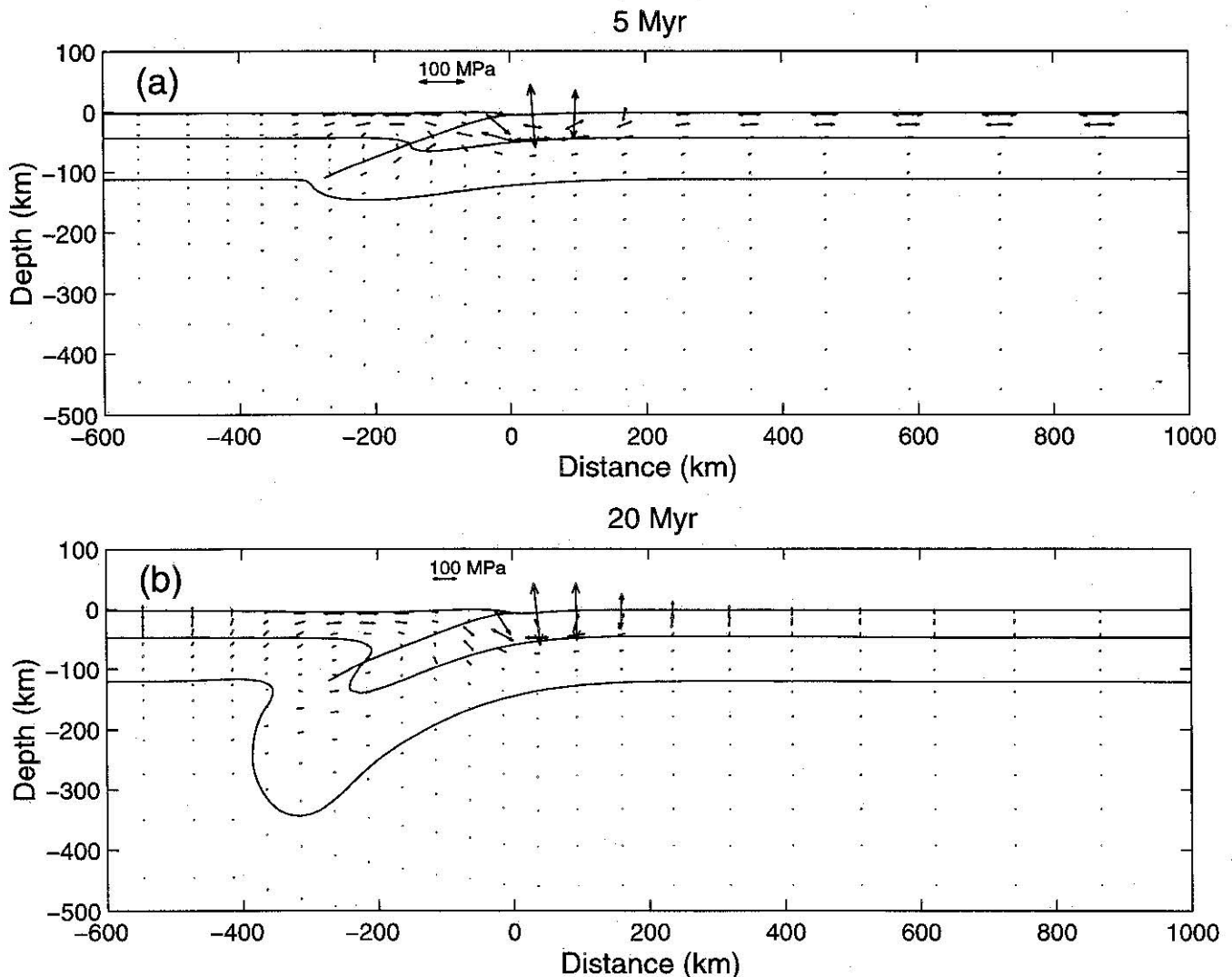


**Figure 4.** Principal deviatoric compressive stress and isotherms for Model A. Isotherms at 600°C intervals. (a) After 5 Myr the horizontal stress within the subducting plate is compressive, ~85 MPa, away from the trench. (b) After 20 Myr the subducting plate is in horizontal extension. Extensional horizontal stresses have also developed within the overriding plate, beyond the slab tip.

### 3.2. Convergence Velocity

We next examined the influence of plate convergence velocity. Topography is compared for three models with different convergence rates which have all been integrated for 10 Myr (Figure 5e). The similarity of the plots shown in Figure 5a and Figure 5e shows that topography is primarily dependent upon depth of slab penetration. When models with different convergence rates are integrated for a total of 400 km of convergence, the models with slower convergence rates have slightly greater slab penetration into the mantle and produce deeper bathymetric depression on the overriding plate (Figure 5f). There is less viscous resistance to the slab penetrating the mantle at a lower velocity. The rates of subsidence are directly proportional to rates of slab penetration and hence to the rate at which the geometry of the buoyancy forces are changing.

### 3.3. Age of Subducting Plate

The thermal age of the lithosphere influences the topography and subsidence rates across the plate boundary. After 20 Myr of convergence at 2 cm/yr, a model with 120 Ma

lithosphere shows a wider and deeper back arc basin and a deeper trench than a model with 40 Ma lithosphere (Figure 6a). The trench depth for 40 Ma lithosphere is 4.5 km while for 120 Ma lithosphere the trench depth has increased to nearly 7.0 km. Subduction of younger lithosphere produces a slower rate of subsidence within the overriding plate (Figure 6b). The average subsidence rate, 250 km from the trench, for a 40 Ma subducting slab is 140 m/Myr. For 120 Ma subducting slab, the subsidence rate increases to 210 m/Myr. It is important to note that for these models the subduction rate is constant at 2 cm/yr. The increase in trench depth, and bathymetry of the overriding plate, with age of subducting slab is due to older lithosphere having a higher-anomalous density and therefore more negative buoyancy. This is supported by flexural isostatic subsidence of the lithosphere.

### 3.4. Mantle Viscosity

Mantle viscosity influences the response of the overriding plate to subduction initiation. Reducing the minimum effective viscosity within the upper mantle from  $6 \times 10^{20}$  Pa s to  $1.6 \times 10^{20}$  Pa s and reducing the viscosity below 670 km to  $1.0 \times 10^{21}$  Pa s increases the bathymetry of the depression

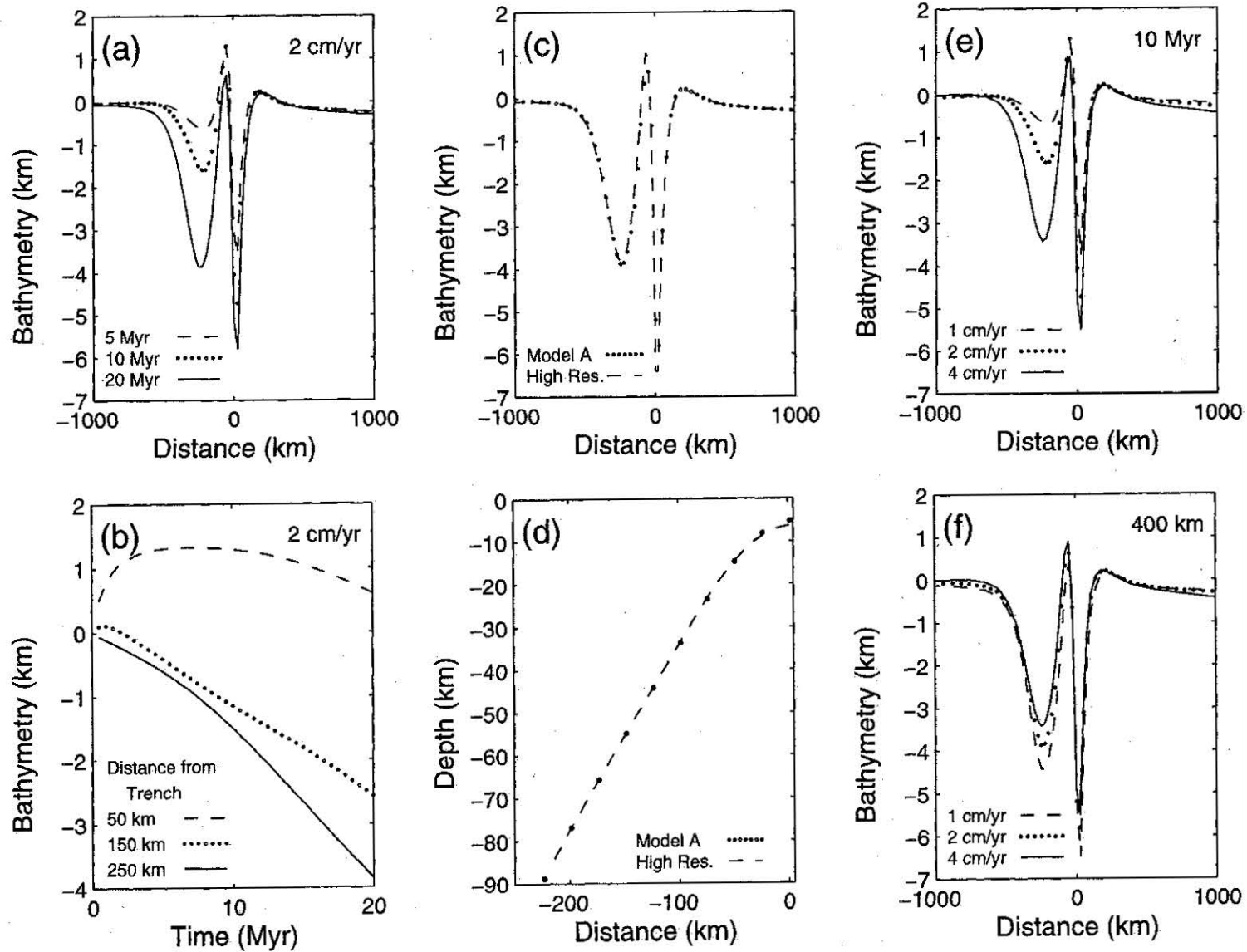


**Figure 5.** (a) Bathymetry across the plate boundary for model A after; 5, 10, and 20 Myr since the initiation of subduction. (b) Subsidence rates for model A within overriding plate 50 150, and 250 km from trench. (c) Bathymetry and (d) fault geometry after 20 Myr, for model A and for the same model but with double the number of elements. (e) Bathymetry after 10 Myr of plate convergence and (f) bathymetry after 400 km of plate convergence at 1, 2, and 4 cm/yr.

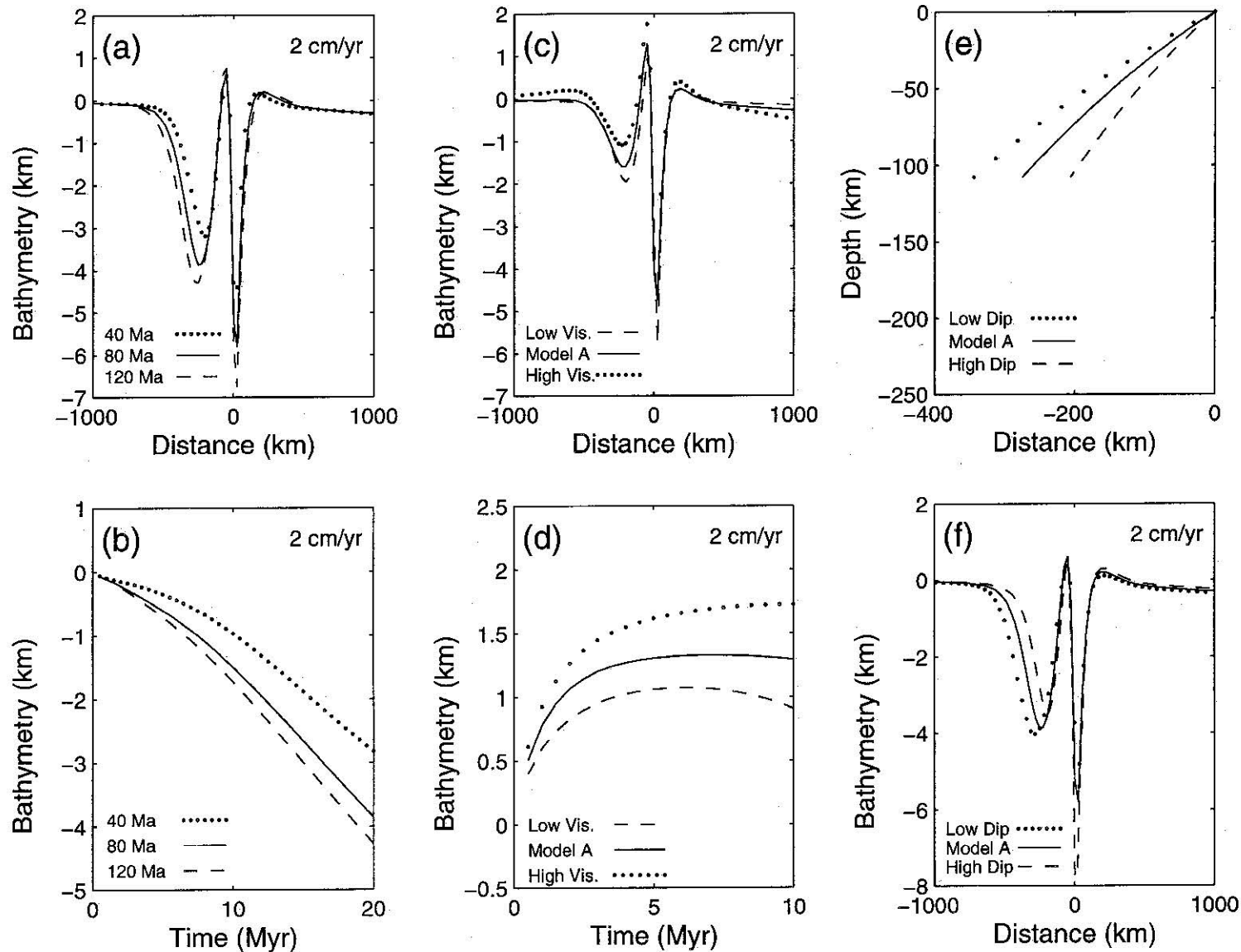


**Figure 6.** (a) Bathymetry and (b) subsidence rates within overriding plate 250 km from trench, for lithosphere which is 40, 80, and 120 Ma. (c) Bathymetry and (d) subsidence within overriding plate 50 km from trench, for model A, and for models in which the upper mantle viscosity has been reduced to  $1.6 \times 10^{20}$  Pa s, and increased to  $1.2 \times 10^{21}$  Pa s. (e) Fault geometry and (f) bathymetry after 20 Myr for model A, and for models with an increased and reduced fault dip.

within the overriding plate, increases trench depth, and reduces the amount of uplift close to the trench (Figure 6c). Increasing the minimum effective viscosity within the upper mantle to  $1.2 \times 10^{21}$  Pa s, and increasing the viscosity below 670 km to  $2.5 \times 10^{22}$  Pa s, reduces the bathymetry within the overriding plate and increases uplift close to the trench (Figure 6d). Uplift increases from 1250 m in model A to 1700 m in the high viscosity model. Since a mantle with a lower viscosity supports a reduced deviatoric stress, for models with a lower viscosity mantle, slab compensation is transferred from the lower boundary of the model to the surface, resulting in an increased bathymetry above the slab.

### 3.5. Fault Geometry

Trench depth is particularly sensitive to changes in the dip of the fault. The fault within model A is curved and has a surface dip of  $17^\circ$  and an average dip of  $23^\circ$  (Figure 6e). If the average fault dip is increased to  $30^\circ$ , then the trench topography, after 20 Myr of convergence at 2 cm/yr, increases dramatically from nearly 6000 m to just under 8000 m. The bathymetric depression within the overriding plate also becomes shallower and more narrow as the compensation for the slab weight is transferred from the overriding plate to the trench. Reducing the average fault dip to  $19^\circ$  reduces the trench depth to <5000 m and produces a deeper and wider bathymetric depression within the overriding plate (Figure 6f). The shallower fault dip increases the vertical coupling between the slab buoyancy and the surface of the overriding plate and therefore results in an increase in the bathymetry of the overriding plate and a reduction in trench depth.

### 3.6. Frictional Failure

In preceding models the deviatoric extensional stress within the upper 10 km of the subducting lithosphere reaches 250 MPa close to the trench (Figure 4b). The maximum shear stress that can be supported by fractured rock within the upper lithosphere is determined from frictional resistance, and is given by Byerlee's law, which holds for a wide range geological materials [Brace and Kohlstedt, 1980],

$$\tau_{\text{yield}} = Kz \quad (5)$$

where  $z$  is depth and  $K$  is dependent upon pore pressure and the mode of faulting. The material is perfectly plastic with a yield stress which is depth dependent. For hydrostatic pore pressure, Brace and Kohlstedt [1980] found that  $K$  is 11.25 MPa/km for extensional stresses and 37.0 MPa/km for compressional stresses. We investigate the influence of frictional failure within the upper lithosphere with  $K$  equal to 10.0 MPa/km (Figure 7), which represents an end member model of minimum failure strength for hydrostatic pore pressure. The maximum deviatoric stresses within the upper 15 km of the lithosphere are reduced (compare Figure 7a with Figure 4b). However, this does not greatly influence the topography (Figure 7b). The maximum trench depth is reduced by 400 m (~7%), and the outer rise migrates slightly toward the trench and is reduced in amplitude. Topography across the plate boundary is insensitive to frictional failure within the upper lithosphere.

### 3.7. Force Boundary Condition

The preceding models all had a constant velocity far field boundary. If, alternatively, a constant force boundary condition is used in a model which is otherwise identical to model A, then the resulting dynamic response of the

overriding plate changes. Ridge push for old oceanic lithosphere is thought to be  $4 \times 10^{12}$  N/m [McKenzie, 1977; Turcotte and Schubert, 1982]. After 5 Myr the principal deviatoric stress for a model with a constant far field force of  $4 \times 10^{12}$  N/m is everywhere compressional, apart from close to the trench where horizontal extension reaches 57 MPa (Figure 8a). After 20 Myr of convergence the slab has reached nearly 250 km depth and the deviatoric compression within the overriding plate, above the fault, has increased to nearly 100 MPa. Within the overriding plate, away from the trench, deviatoric stresses have changed from compression at 5 Myr to extension at 20 Myr. The velocity of the subducting plate for a model with a plate force of  $4 \times 10^{12}$  N/m is initially 9 mm/yr and increases to 24 mm/yr by 20 Myr as the slab develops and slab pull increases (Figure 9a). The subsidence rate within the overriding plate also increases rapidly from 50 m/Myr initially to over 200 m/Myr as the slab develops and the subduction rate increases (Figure 9b). For a model with a plate force of  $6 \times 10^{12}$  N/m, the initial convergence velocity is 14 mm/year (Figure 9a); this increases to almost 120 mm/year after 20 Myr, by which time the slab has reached 500 km depth. A plate force of  $2 \times 10^{12}$  N/m, produces an initial

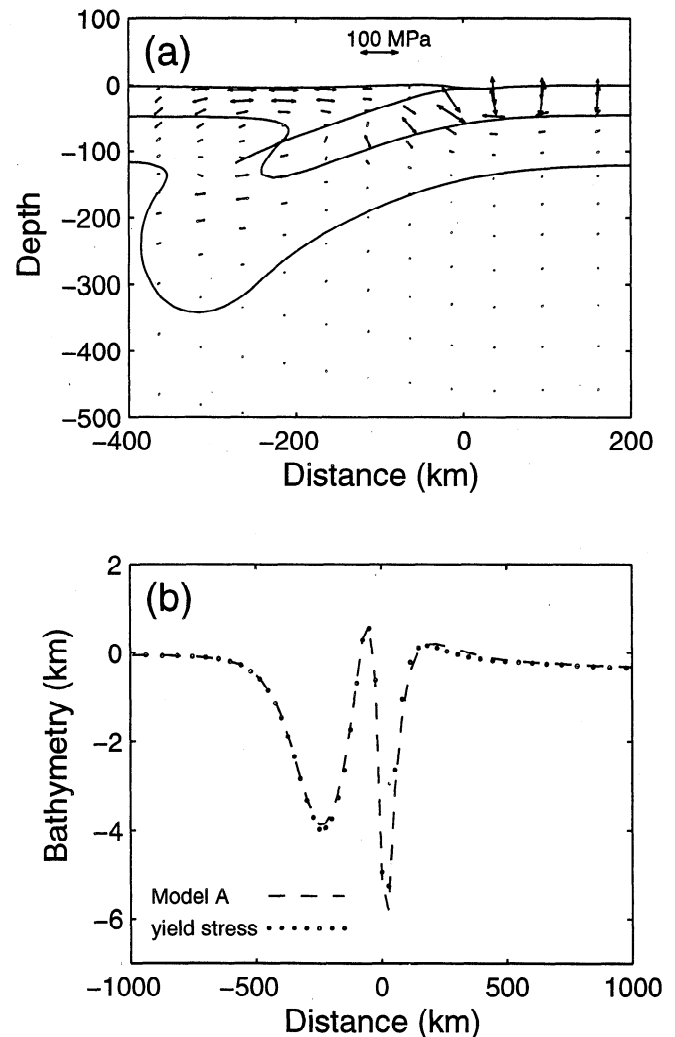
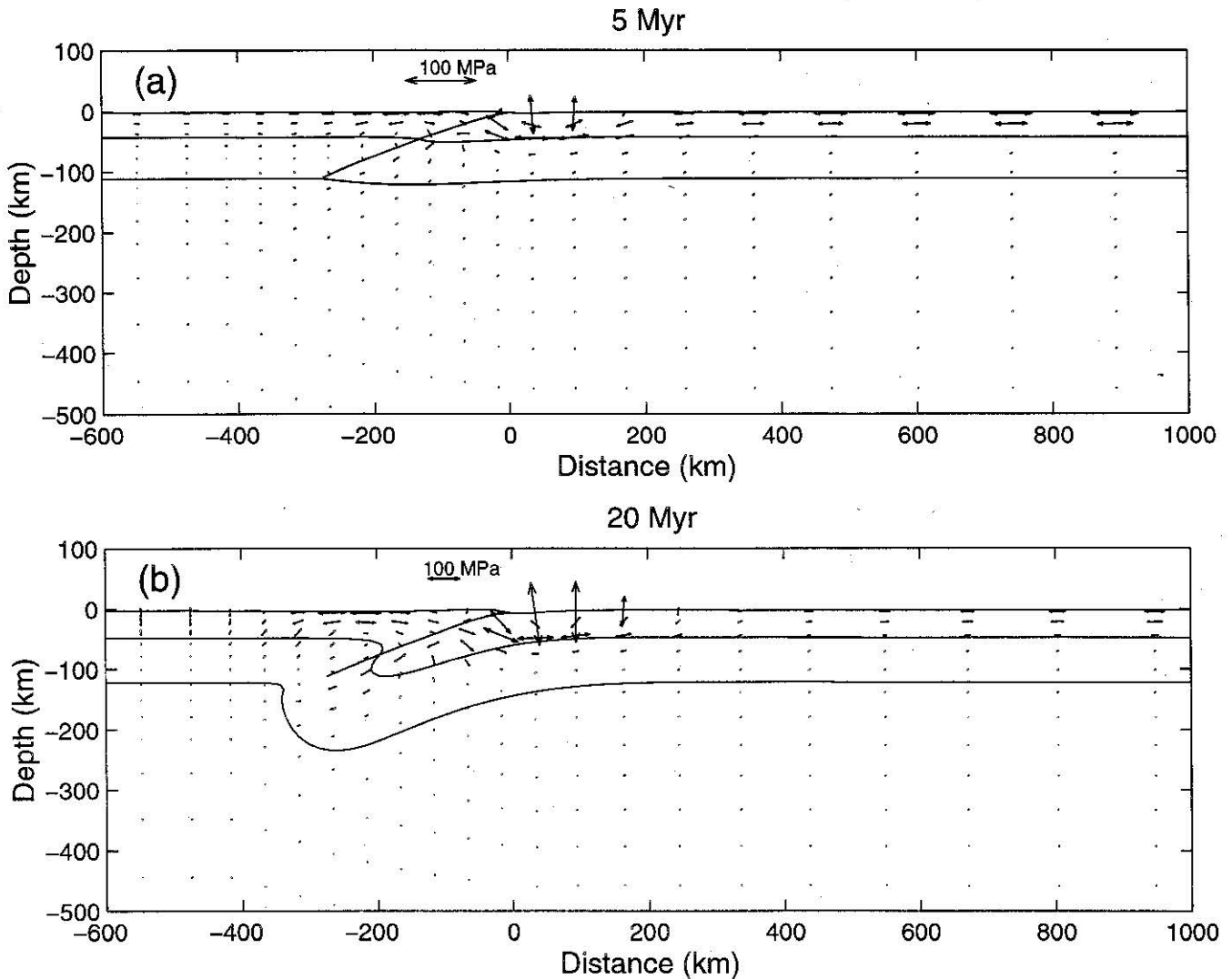


Figure 7. (a) Deviatoric compressional stress for a model identical to model A but with frictional failure governed by Byerlee's Law with a yield strength gradient of 10 MPa/km. (b) The corresponding topography after 20 Myr compared with model A.



**Figure 8.** Principal deviatoric compressive stress and isotherms for the model with a constant force boundary of  $4 \times 10^{12}$  N/m. Isotherms at  $600^\circ\text{C}$  intervals. (a) After 5 Myr, little convergence has taken place, and horizontal compression dominates the stress field within both the overriding and subducting plates. (b) After 20 Myr, convergence rate has increased, and the slab is now well developed. Downdip compression is seen within the slab, and horizontal extension is seen within the overriding plate away from the trench.

convergence velocity of 4 mm/yr. This does not increase substantially with time (Figure 9a). After 20 Myr the  $1200^\circ\text{C}$  geotherm has been perturbed downward by  $<40$  km; the rate of convergence is so low that diffusive heating does not allow a slab to develop, and we conclude that subduction will not start for a significantly longer period of time.

### 3.8. Frictional Resistance of Fault Plane

We can incorporate a shear stress on the fault, within the lithosphere, by increasing the shear stiffness there (Figure 2). In this way a shear stiffness is initially imposed, and the resulting shear stress on the fault is calculated from the fault displacement, after the model has been run. For a constant plate force of  $6 \times 10^{12}$  N/m, increasing the shear stress on the fault from zero to 8.8 MPa reduces the initial convergence velocity from 14 mm/yr to 9 mm/yr (Figure 9c). The high shear stress prevents subduction from becoming well established, the convergence velocity after 20 Myr has only increased to 12 mm/yr. This is in contrast to the model with

zero shear stress, which shows a rapid increase in convergence velocity to 120 mm/yr after 20 Myr. After 200 km of plate convergence a fault with zero shear stress produces a bathymetric depression on the overriding plate with a maximum depth of 1500 m. Increasing the shear stress on the fault produces a depression with a significantly shorter wavelength and increases the bathymetry to 2000 m (Figure 9d). However, the increase in fault shear stress does not greatly influence the amount of uplift close to the fault. Therefore increasing the fault shear stress has two major effects. First, it retards the rate of plate convergence for a constant plate force, and second, it produces greater bathymetry in a basin on the overriding plate which is narrower and closer to the trench (Figure 9d).

### 3.9. Conditions for Subduction Initiation

In order to assess the conditions necessary to allow subduction to initiate, we have explored the parameter space of plate force versus fault resistance, for models that have

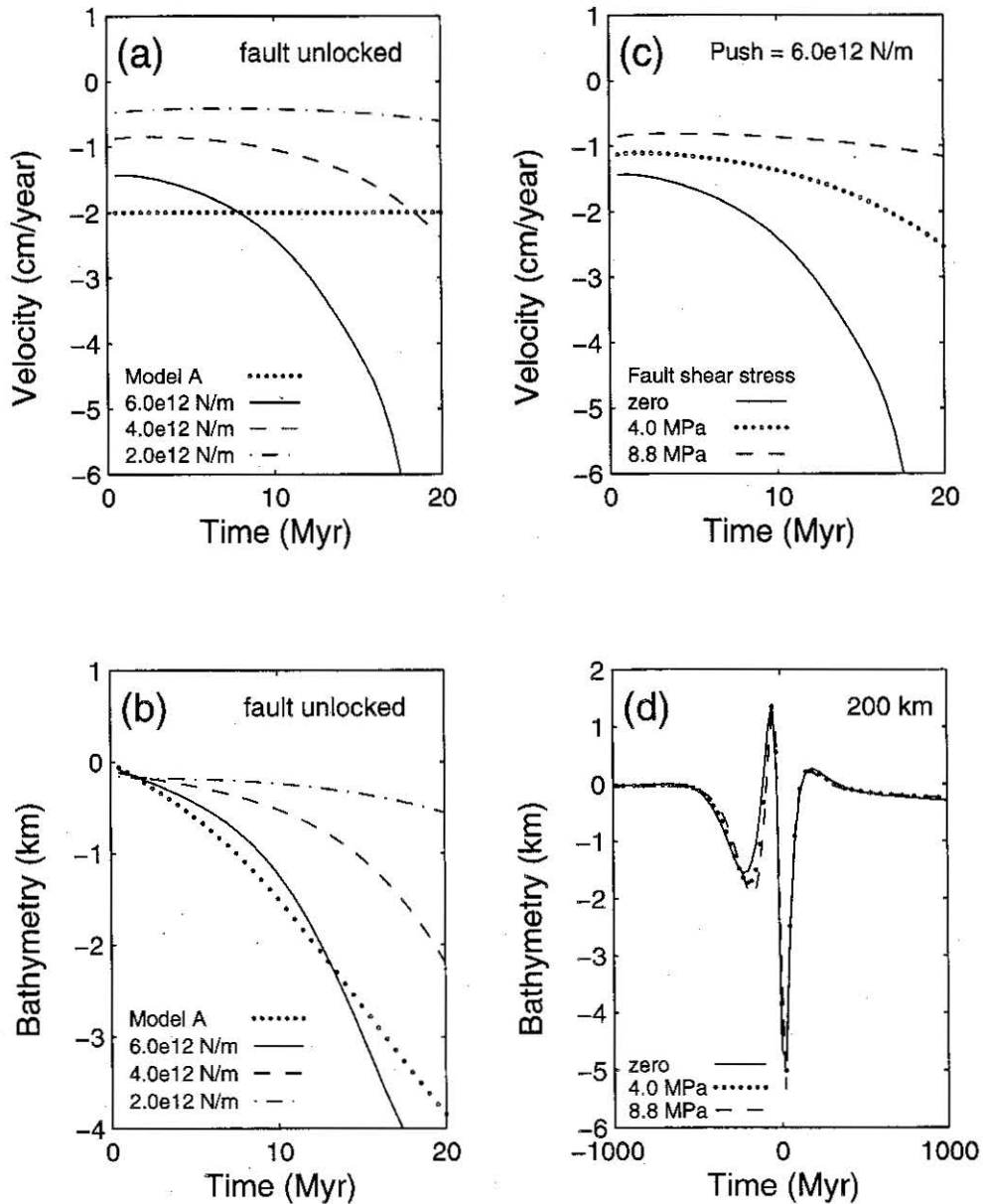


**Figure 9.** (a) Convergence velocity and (b) bathymetry 250 km from the trench for models with a far field force of  $2 \times 10^{12}$  N/m,  $4 \times 10^{12}$  N/m,  $6 \times 10^{12}$  N/m, and Model A. (c) Convergence velocity and (d) bathymetry after 200 km of convergence for models with a far field force of  $6 \times 10^{12}$  N/m and a fault shear stress of zero, 4.0 MPa, and 8.8 MPa.

been integrated for 20 Myr. Convergence velocities increase with increasing plate force and decreasing fault resistance, as expected (Figure 10). There is no simple criteria to determine that subduction has not initiated. However, we found that models which proceeded with a convergence rate of  $<10$  mm/yr did not show the later increase in subduction rate that models with a higher velocity displayed within the 20 Myr time interval. We concluded that at subduction velocities of  $<10$  mm/yr thermal diffusion inhibits slab formation and no substantial slab pull force develops. Therefore we judged that if the convergence velocity has not reached 10 mm/yr after 20 Myr, then subduction has failed to initiate and is unlikely to do so. For a plate force of  $4 \times 10^{12}$  N/m, subduction initiates when the fault shear stress is  $<3$  MPa. Subduction fails to initiate when the fault shear stress is greater than 5 MPa (Figure 10). For a plate force of  $6 \times 10^{12}$  N/m, then subduction will initiate when the fault shear stress is  $<9$  MPa. When the

plate force is only  $2 \times 10^{12}$  N/m, subduction fails to initiate when there is zero shear stress on the fault. From the criteria for initiation discussed above, then we find that subduction will initiate if

$$\tau_{\max} < 3.1 \times 10^{-12} \times F_{PF} - 8.5 \text{ MPa} \quad (6)$$

where  $F_{PF}$  is the plate force (N/m) and  $\tau_{\max}$  is the maximum shear stress (MPa) on a preexisting fault.

#### 4. Discussion and Conclusions

There are two fundamental results of this systematic investigation of subduction initiation in which oceanic lithosphere has a preexisting dipping fault. First, we have more precisely determined the forces necessary to initiate

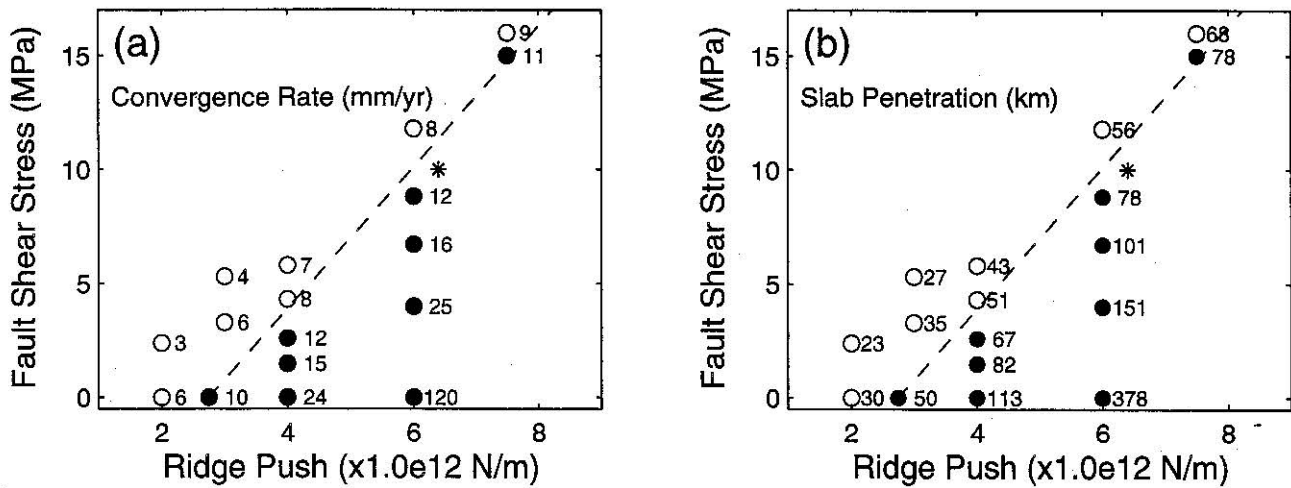


**Figure 10.** Fault shear stress plotted against plate force (a) with plate convergence velocity (mm/yr) after 20 Myr indicated and (b) with depth of slab penetration (km) indicated. Subduction is deemed to have successfully started when the convergence rate exceeds 10 mm/yr (solid circles). Subduction has not initiated when the convergence velocity is <10 mm/yr (open circles). Also shown is *McKenzie's* [1977] estimate (star).

subduction, and second, we have determined the evolutionary sequence of tectonic events which occur as initiation proceeds. The first set of results is necessary to determine why, where, and how subduction initiates, while the second set is necessary to tie model dynamics to specific sites of initiation with geological and tectonic constraints. We will turn to each of these aspects.

We find that subduction can initiate for a reasonable set of Earth parameters and, as we will see, does not appear to be nearly as difficult as some studies have previously concluded. Our results are best summarized in Figure 10 and by equation (6) which separate the no initiation and initiation fields. In the domain above the line, subduction will not initiate because convergence is so small that only a small deflection of the lithosphere occurs in 20 Myr. While in the lower domain, subduction clearly initiates as the slab pull force becomes unmistakable by or before 20 Myr. In Figure 10 we have included *McKenzie's* [1977] estimate for the force necessary to initiate subduction, which is consistent with our results for a fault with the same shear stress. *McKenzie* [1977] required a convergence rate of 13 mm/yr for subduction to be initiated which is also quite consistent with our direct calculations (Figure 10a). However, *McKenzie* [1977] argued that ridge push forces were unlikely to be  $>4 \times 10^{12}$  N/m, and since his estimate of the force necessary to initiate subduction was greater than this, he argued that initiation was unlikely to occur by ridge push alone. *Mueller and Phillips* [1991] also set up a model quite similar to *McKenzie* [1977] but found that the force required to initiate subduction was  $>40 \times 10^{12}$  N/m, far in excess of our estimates, because of their inclusion of extraordinarily large resisting stresses on preexisting faults. It should be pointed out that in all three studies, *McKenzie* [1977], *Mueller and Phillips* [1991], and our present numerical model, an inclined, preexisting fault completely cutting the oceanic lithosphere was included in the model.

Do reasonable Earth parameters fall within the subduction initiation or no initiation domain (Figure 11)? Ridge push forces for 100 Ma lithosphere and 3 km of subsidence are in the range of  $2.0 \times 10^{12}$ – $4.0 \times 10^{12}$  N/m (Figure 11) [*Bott*, 1991; *McKenzie*, 1977; *Fleitout and Froidevaux*, 1983; *Turcotte and Schubert*, 1982]. With large amounts of slab pull available for those plates in ocean basins such as the Pacific, these ridge push forces are clearly minimum estimates of the forces available to initiate subduction. However, even without

additional forces, subduction initiation is still possible (Figure 11) as the stress drop in large interplate earthquakes are on average 3 MPa [*Kanamori*, 1980], although there is still scatter in the estimates between 1 and 10 MPa representing real variation in stress drop. Such stress drops may not reflect the absolute value of stress across large fault zones rather only the stress released during the earthquake. However, estimates of absolute stress across the San Andreas transform fault in California must be  $<10$  MPa because of the lack of a heat flow anomaly in the vicinity of the fault [*Lachenbruch and Sass*, 1988]. The weakness of the San Andreas fault is corroborated by the complete absence of right lateral shear as inferred from stress measurement in deep boreholes [*Zoback and Healy*, 1992]. Such estimates are consistent with 10–30 MPa absolute shear stresses on faults inferred from a comparison between dynamic models of trenches driven by the buoyancy of slabs and trench depths at ocean-ocean converging margins [*Zhong and Gurnis*, 1992, 1994]. Consequently, even with ridge push forces alone, we find that subduction can initiate. Moreover, with the additional force available from adjacent subduction zones, increasing the driving force above  $4 \times 10^{12}$  N/m, subduction initiation is not difficult, and we would predict it to be a common phenomena, especially in the western Pacific where it has happened repeatedly over the Mesozoic and Cenozoic. The most significant limitation of the present estimate is the inclusion of an inclined fault as opposed to a vertical fault which would be expected if the original fault were a transform fault. This can only be addressed with a more sophisticated approach incorporating fault growth. Development of reverse faults occur directly adjacent to strike-slip faults during subduction initiation as observed on the evolving Puysegur ridge south of the South Island of New Zealand [*Collot et al.*, 1995].

In addition to the conditions necessary to initiate subduction, we have studied in detail the evolution of topography across the plate boundary as subduction developed. Uplift and subsidence history may be preserved in the geological record, allowing us to use the model to investigate the dynamics of specific sites of initiation. It was found that the topography across a convergent margin is dependent upon the depth of slab penetration, the age of the slab, mantle viscosity, and fault dip. Of these parameters, depth of slab penetration is clearly the most important.

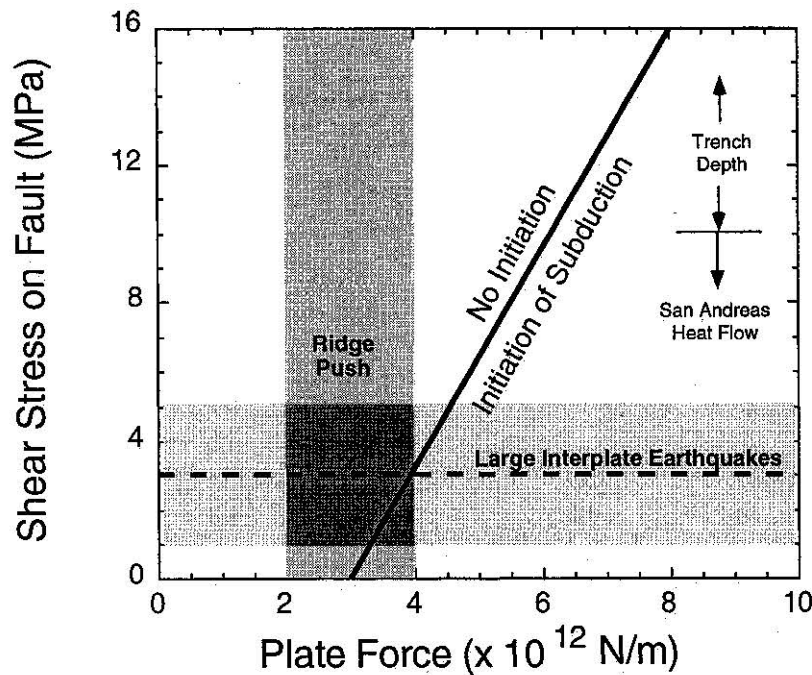


**Figure 11.** Comparison of theoretical prediction of the boundary between the domains of subduction initiation and no initiation (heavy solid line) from equation (6). Range of ridge push forces are discussed in text. Shear stresses on preexisting faults from three different estimates are indicated: large interplate earthquakes from [Kanamori, 1980], from heat flow on San Andreas fault [Lachenbruch and Sass, 1988], and from trench depths [Zhong and Gurnis, 1992, 1994].

Whether the slab penetrates to a set depth quickly (as it would with a high-subduction velocity) or slowly (as it would with a low-subduction velocity) does not substantially influence the topography of either the overriding plate or the trench. This is an important result because it indicates that the instantaneous density distribution within the mantle largely determines the topography. Trench depth and overriding plate bathymetry increase with older subducting slabs and smaller mantle viscosity. As the compensation for the weight of the slab was transferred from the overriding plate to the trench, a larger fault dip was found to cause deeper trenches but shallower bathymetry on the overriding plate. Increasing mantle viscosity increases initial uplift within the overriding plate close to the trench.

As subduction initiates a long wavelength bathymetric depression develops on the overriding plate with a wavelength of ~400 km and a maximum depth 250 km from the trench. For a convergence velocity of 2 cm/yr, initial subsidence rates are 125 m/Myr. This agrees well with subsidence rates recorded on the North Island of New Zealand, where subduction initiated in the early Miocene, and the convergence rate was <20 mm/year [Walcott, 1987]. Stern and Holt [1994] analyzed well-hole paleobathymetric data and noted long-wavelength subsidence within the South Taranaki basin, coincident with the initiation of subduction beneath the North Island, with an average subsidence rate of 130 m/Myr at a distance of ~300 km from the trench. The initiation of subduction beneath the North Island of New Zealand was also accompanied by an ~5 Myr episode of compression, thrust sheet emplacement, and uplift close to the trench [Rait et al., 1991]. Our models predict rapid uplift close to the trench during the first 5 Myr, followed by a subsequent slow subsidence (Figure 5b). Upon the onset of convergence, the overriding plate immediately goes into horizontal compression directly above the fault. For the model with a convergence velocity of 2 cm/yr this

compression increases from 53 MPa at 5 Myr to 85 MPa at 20 Myr. Extensional stresses are seen within the overriding plate beyond the slab tip. These extensional stresses were originally zero but reach 55 MPa after 20 Myr. The slab tip appears to mark the boundary between compressional and extensional deviatoric stresses within the overriding plate. Down-dip compression is initially seen within the slab after 100 km of convergence but this changes to down-dip extension after 400 km of convergence. Therefore the plate boundary is initially dominated by compressional stresses, but as subduction proceeds, extensional stresses develop both within the slab and within the overriding plate.

The amplitude of the topography within the overriding plate after 400 km of convergence was very similar to that predicted by Zhong and Gurnis [1994] for a purely viscous, steady-state model. The relationships observed here, between plate age and trench depth and between fault dip and trench depth, were also found by Zhong and Gurnis [1994]. However, our viscoelastic model predicts longer wavelength subsidence, probably reflecting the elastic flexure of upper lithosphere. The viscoelastic model leads to trench depths which are >1000 m deeper than that predicted by Zhong and Gurnis [1994]. The minimum effective viscosity within the mantle is similar for both models, ~ $5 \times 10^{20}$  Pa s. The elastic upper lithosphere within the viscoelastic model may more efficiently transmit stress from the slab to the surface.

Kanamori [1980] estimated an average fault shear stress drop of 3-6 MPa for large earthquakes from seismic moment, with a maximum shear stress of <10 MPa. For a ridge push force of  $4 \times 10^{12}$  N/m, subduction can initiate if the fault shear stress is 3 MPa or less. Therefore our results suggest that subduction initiation within oceanic basins across preexisting weak zones is entirely consistent with estimates of ridge push and fault shear stress. The results show that subduction initiation will not occur readily in all oceanic basins. Subduction initiation is likely where older oceanic

basins are intersected by faults with low shear stress or on faults with higher shear stress, where the resultant plate boundary force is higher than ridge push alone.

**Acknowledgments.** We thank Mark Simons for helpful comments on the manuscript. This work was supported by NSF grant EAR-9614391 and represents contribution 6281 of the Division of Geological and Planetary Sciences, California Institute of Technology.

## References

- Bott, M.H.P., Ridge push and associated plate interior stress in normal and hot spot regions, *Tectonophysics*, 200, 17-32, 1991.
- Bott, M.H.P., G.D. Waghorn, and A. Whittaker, Plate boundary forces at subduction zones and trench-arc compression, *Tectonophysics*, 170, 1-15, 1989.
- Brace, W. F., and D.L. Kohlstedt, Limits on lithospheric stress imposed by laboratory experiments, *J. Geophys. Res.*, 85, 6248-6252, 1980.
- Brooks, A. N., A Petrov-Galerkin finite element formulation for convection dominated flows, Ph.D. thesis, Calif. Inst. Tech., Pasadena, 1981.
- Casey, J.F., and J.F. Dewey, Initiation of subduction zones along transform and accreting plate boundaries, triple-junction evolution, and forearc spreading centres—implications for ophiolitic geology and obduction, in *Ophiolites and Oceanic Lithosphere*, edited by I.G. Gass, S.J. Lippard, and A.W. Shelton, Geol. Soc. Spec. Publ. 13, 269-290, 1984.
- Cloetingh, S., R. Wortel, and N.J. Vlaar, On the initiation of subduction zones, *Pure Appl. Geophys.*, 129, 7-25, 1989.
- Collot, J.-Y., G. Lamarche, R.A. Wood, J. Delteil, M. Sosson, J.-F. Lebrun, and M.F. Coffin, Morphostructure of an incipient subduction zone along a transform plate boundary: Puysegur ridge and trench, *Geology*, 23, 519-522, 1995.
- Copper, A.K., D.W. Scholl, and M.S. Marlow, Plate tectonic model for the evolution of the eastern Bering Sea Basin, *Geol. Soc. Am. Bull.*, 87, 1119-1126, 1976.
- Courtney, R.C., and C. Beaumont, Thermally activated creep and flexure of the oceanic lithosphere, *Nature*, 305, 201-204, 1983.
- Fleitout, L., and C. Froidevaux, Tectonic stresses in the lithosphere, *Tectonics*, 2, 315-324, 1983.
- Forte, A.M., and J.X. Mitrovica, New inferences of mantle viscosity from joint inversion of long-wavelength mantle convection and post-glacial rebound data, *Geophys. Res. Lett.*, 23, 1147-1150, 1996.
- Goodman, R.E., R.L. Taylor, and T.L. Brekke, A model for the mechanics of jointed rock, *J. Soil Mech. Found. Div. Am. Soc. Civ. Eng.*, 94, 637-658, 1968.
- Gurnis, M., Rapid continental subsidence following the initiation and evolution of subduction, *Science*, 255, 1556-1558, 1992.
- Gurnis, M., and B.H. Hager, Controls on the structure of subducting slabs, *Nature*, 335, 317-321, 1988.
- Hegarty, K.A., J.K. Weisell, and D.E. Hayes, Convergence at the Caroline-Pacific plate boundary: Collision and subduction, in *The Tectonic and Geological Evolution of Southeast Asian Seas and Islands, Part 2*, *Geophys. Monogr. Ser.*, vol. 27, edited by D.E. Hayes, pp. 326-348, AGU, Washington, D. C., 1982.
- Hilde, T.W.C., S. Uyeda, and L. Kroenke, Evolution of the western Pacific and its margin, *Tectonophysics*, 38, 145-165, 1977.
- Kamp, P.J.J., Neogene and Quaternary extent and geometry of the subducted Pacific plate beneath North Island, New Zealand: Implications for Kaikoura tectonics, *Tectonophysics*, 108, 241-266, 1984.
- Kanamori, H., The state of stress in the Earth's lithosphere, in *Physics of the Earth's Interior*, edited by A. Dziewonski and E. Boschi, pp. 531-554, North-Holland, New York, 1980.
- Karig, D.E., Initiation of subduction zones: Implications for arc evolution and ophiolite development, in *Trench-Forearc Geology: Sedimentation and Tectonics on Modern and Ancient Active Plate Margins*, edited by J. K. Leggett, Geol. Soc. Spec. Publ., 10, 563-576, 1982.
- Kemp, D.V., and D.J. Stevenson, A tensile flexural model for the initiation of subduction, *Geophys. J.*, 125, 73-94, 1996.
- Lachenbruch, A.H., and J.H. Sass, The stress-heatflow paradox and thermal results from Cajon Pass, *Geophys. Res. Lett.*, 15, 981-984, 1988.
- McKenzie, D.P., The initiation of trenches: A finite amplitude instability, in M. Talwani, and W. C. Pittman, *Island Arcs, Deep Sea Trenches, and Back-Arc Basins, Maurice Ewing Ser.*, Vol. I, pp. 57-61, AGU, Washington, D. C., 1977.
- Melosh, H.J. and A. Raefsky, The dynamic origin of subduction zone topography, *Geophys. J. R. astr. Soc.* 60, 333-354, 1980.
- Melosh, H.J., and C.A. Williams Jr., Mechanics of graben formation in crustal rocks: A finite element analysis, *J. Geophys. Res.*, 94, 13,961-13,973, 1989.
- Mueller, S., and R.J. Phillips, On the initiation of subduction, *J. Geophys. Res.*, 96, 651-665, 1991.
- Rait, G., F. Chanier, and D. Waters, Landward and seaward-directed thrusting accompanying the onset of subduction beneath New Zealand, *Geology*, 19, 230-233, 1991.
- Ranalli, G., *Rheology of the Earth*, 413 pp., Chapman and Hall, New York, 1995.
- Ruff, L., and H. Kanamori, Seismic coupling and uncoupling at subduction zones, *Tectonophysics*, 99, 99-117, 1983.
- Scholl, D.W., E.C. Buffington, and M.S. Marlow, Plate tectonics and the structural evolution of the Aleutian-Bering Sea region, *Spec. Pap. Geol. Soc. Am.*, 131, 1-31, 1975.
- Stern, J.R., and S.H. Bloomer, Subduction zone infancy: Examples from the Eocene Izu-Bonin-Mariana and Jurassic California arcs, *Geol. Soc. Am. Bull.*, 104, 1621-1636, 1992.
- Stern, T.A., and W.E. Holt, Platform subsidence behind an active subduction zone, *Nature*, 368, 233-236, 1994.
- Turcotte, D.L., and G. Schubert, *Geodynamics: Applications of Continuum Physics to Geological Problems*, 450 pp., John Wiley, New York, 1982.
- Uyeda, S., and Z. Ben-Avraham, Origin and development of the Philippine Sea, *Nature Phys. Sci.*, 240, 176-178, 1972.
- Walcott, R.I., The kinematics of the plate boundary zone through New Zealand: A comparison of short and long term deformations, *Geophys. J. R. Astr. Soc.*, 79, 613-633, 1984.
- Wallace, M.H., and H.J. Melosh, Buckling of a pervasively faulted lithosphere, *Pure Appl. Geophys.*, 142, 239-261, 1994.
- Watts, A. B., J.H. Bodine, and M.S. Steckler, Observations of flexure and the state of stress in the oceanic lithosphere, *J. Geophys. Res.*, 85, 6369-6376, 1980.
- Wdowinski, S., and R. O'Connell, Deformation of the Central Andes (15°-27°S) derived from a flow model of subduction zones, *J. Geophys. Res.* 96, 12,245-12,255, 1991.
- Wdowinski, S., and Y. Bock, The evolution of deformation and topography of high elevated plateaus, 1, Model, numerical analysis, and general results, *J. Geophys. Res.*, 99, 7103-7119, 1994.
- Zhong, S., and M. Gurnis, Viscous flow model of a subduction zone with a faulted lithosphere: Long and short wavelength topography, gravity, and geoid, *Geophys. Res. Lett.*, 19, 1891-1894, 1992.

- Zhong, S., and M. Gurnis, Controls on trench topography from dynamic models of subduction zones, *J. Geophys. Res.*, 99, 15,683-15,695, 1994.
- Zienkiewicz, O.C., *The Finite Element Method*, 787 pp., McGraw-Hill, New York, 1977.
- Zoback, M.D., and J.H. Healy, In situ stress measurements to 3.5 km depth in the Cajon Pass scientific research borehole: Implications for the mechanics of crustal faulting, *J. Geophys. Res.*, 97, 5039-5057, 1992.

---

M. Gurnis, Seismological Laboratory 252-21, California Institute of Technology, Pasadena, CA 91125. (e-mail: gurnis@gps.caltech.edu.)

J. Toth, Shell International Exploration and Production, Rijswijk, Netherland. (e-mail: J.TOTH@siep.shell.com.)

(Received October 8, 1997; revised February 27, 1998; accepted March 19, 1998.)